Robotica (2026), **44**, pp. 764–782
doi:10.1017/S0263574726103312

CAMBRIDGE UNIVERSITY PRESS

RESEARCH ARTICLE

Enabling physical human/dual-arm collaboration to resist random impacts: An improved shear-thickening fluid controller

Siwen Zhang[1], Jinjun Duan[1], Kai Gui[2], Yiming Bin[1], Chendong Wu[1], Yanzhao Yu[1], Tingyan Du[1], Zhengwei Wang[1], Lingyu Wang[1] and Hongtao Wu[1]

[1]Nanjing University of Aeronautics and Astronautics College of Mechanical and Ele, China
[2]Shanghai Jiao Tong University School of Mechanical Engineering, China
Corresponding author: Jinjun Duan; Email: duan-jinjun@nuaa.edu.cn

Received: 14 May 2025; **Revised:** 9 November 2025; **Accepted:** 13 December 2025; **First published online:** 30 March 2026

Keywords: physical human–robot interaction; human/dual-arm robot collaboration; improved shear thickening fluid control; nonlinear random impact disturbances

Abstract

Physical human–robot collaboration (pHRC) has gained significant traction in industrial settings due to its exceptional flexibility and adaptability. However, robots often face unexpected nonlinear and random impact disturbances during task execution, which pose risks such as human injury and robotic instability. To address these challenges, this paper proposes a novel control strategy based on improved shear-thickening fluid control (ISFC) for enhancing human–robot cooperation. Drawing inspiration from the unique properties of shear-thickening fluids, ISFC is designed to ensure stable collaboration between humans and robots while effectively mitigating the effects of random impacts. Furthermore, an ISFC-based framework is introduced for human/dual-arm robot collaboration. Comprehensive simulations and experimental evaluations are conducted to validate the effectiveness and advantages of the proposed approach. The experimental results show that compared with the traditional linear admittance control (L-AC) and SFC, ISFC not only has excellent impact resistance (peak velocity <0.1 m/s under 30 N impacts) but also overcomes the stability defects of SFC in low-speed operation, reducing the convergence time by 94.1% (from 8.29 s to 0.50 s) and residual displacement by 49.3% (from 13.21 mm to 6.7 mm). In dual-arm collaboration, the position synchronization error remains below 8 mm. These improvements provide a new idea for the application of human–robot collaboration.

1. Introduction

Humanoid robots, capable of emulating humans in performing complex tasks, have become indispensable in fields such as industrial automation [1, 2], healthcare [3], and home services [4, 5]. Among the essential technologies for humanoid robots, achieving dexterous upper-limb control is crucial. However, current dual-arm robots encounter significant challenges related to dexterity, flexibility, and adaptability [6, 7].

Integrating human intelligence into a dual-arm closed-loop system holds promise for overcoming these challenges. Physical human–robot collaboration (pHRC) fosters inclusive and interactive collaboration by merging human and dual-arm robotic strengths. Utilizing physical feedback, robots can discern human intentions and adjust their actions in real time, facilitating seamless human–robot integration [8, 9]. However, nonlinear impact disturbances, such as unconscious movements, collisions, or operational errors during collaboration, may destabilize robots, causing actions like shaking or jumping, which jeopardize safety.

Compliance control is a widely acknowledged solution to these challenges, with impedance and admittance control being predominant approaches [10, 11]. Impedance control relies on precise dynamic

© The Author(s), 2026. Published by Cambridge University Press.

https://doi.org/10.1017/S0263574726103312 Published online by Cambridge University Press

parameter identification and nonlinear control, yet many collaborative robots use current estimation for torque-based impedance control, leading to suboptimal performance [12, 13]. Admittance control, which uses force/torque sensors for direct contact force detection, is currently the most effective and widely adopted method [14, 15]. However, traditional admittance control employs fixed parameters, lacking adaptability to dynamically track changes in human intentions [16, 17]. To address this, force classification logic based on human intention perception has been developed, along with adaptive variable admittance methods that consider inertial forces to enable compliant interaction [18, 19]. Although these methods enhance alignment with human intentions, they do not fully mitigate nonlinear impact disturbances. Some studies employ signal threshold filtering and mathematical model matching to distinguish collision forces from expected contact forces [20, 21]. However, these approaches are limited by time delays and recovery errors, adversely affecting real-time responsiveness and accuracy in human–robot collaboration. Additionally, research [22] identifies collisions based on force magnitude, effectively detecting collisions but causing immediate cessation of system operations, which fails to provide shock resistance during tasks.

To address these challenges, a novel shear-thickening fluid controller (SFC) was proposed in ref. [23], enabling robots to effectively resist external impact forces while complying with traction forces. The controller exploits the solid–liquid phase transition properties of shear-thickening fluids (STFs), which rapidly increase viscosity under high shear stress, enhancing system damping characteristics for shock absorption and cushioning. This approach has proven successful in machining applications [24, 25]. However, analyses and experiments revealed limitations; the STF-based controller relies solely on shear-thickening properties, neglecting insufficient viscosity under low shear stress conditions. Consequently, upon traction force removal, robots may continue movement at low speeds, leading to inaccuracies and safety concerns. Furthermore, this control method is not directly applicable to closed-chain systems like dual-arm robots. In human/dual-arm robot collaboration, addressing both random external forces and coordinated dual-arm synergy is essential. These limitations constrain the application and development of human/dual-arm collaboration across various domains.

The remainder of this paper is organized as follows. Section II reviews the applications and limitations of linear admittance control (L-AC) and SFC in pHRC. Section III discusses the design of the improved shear thickening fluid control (ISFC) and analyzes its stability and dynamic characteristics. Sections IV and V present the simulation and experimental results, respectively, validating the superiority of the proposed ISFC method. Finally, Section VI concludes the paper.

2. A pHRC framework based on virtual dynamics control

2.1. Physical human–robot collaboration framework

The essence of pHRC lies in enabling robots to emulate the dynamic characteristics of real-world physical systems by adjusting the virtual dynamic relationship between input forces and output displacements within the system. For instance, admittance control facilitates human–robot interaction by allowing the robot to simulate the behavior of a second-order spring-damping system. A framework for human–robot collaboration based on force controller module is illustrated in Figure 1. This framework comprises three key modules: the force control layer, the robot lower-level control Layer, and the pHRC Module [23].

The force control layer is mainly composed of load identification, gravity/inertial force compensation module, and force controller. Among them, the force controller generates the appropriate velocity $\mathbf{x}(t)$ based on the external force $\mathbf{f}_{ext}$. This module can be implemented using L-AC, characterized by a second-order spring-damping system, and can also extend to simulate other physical processes, such as shear-thickening fluid dynamics.

The robot lower-level control layer primarily consists of an inverse kinematics solver, a servo controller, and the robot mechanical system. After calculating the robot's position command in Cartesian space, the desired joint angle $\mathbf{q}_d$ is determined via the inverse kinematics solver, which supplies joint position commands to the servo controller. The controller, in turn, generates the necessary joint torques $\boldsymbol{\tau}$, based on the velocity commands to drive the robot towards the desired velocity and position.

https://doi.org/10.1017/S0263574726103312 Published online by Cambridge University Press

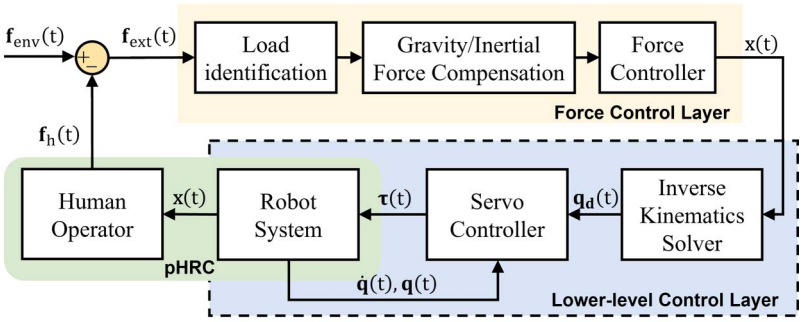


Figure 1. *Schematic diagram of pHRC framework.*

The inverse kinematics solver typically employs the inverse Jacobian matrix approach to establish the relationship between the joint velocities and the end-effector velocities, as expressed in the following equations:

$$\begin{aligned} \mathbf{x}\,(t) &= \mathbf{J}\,(\mathbf{q}\,(t))\,\dot{\mathbf{q}}\,(t) \\ \dot{\mathbf{q}}\,(t) &= \mathbf{J}(\mathbf{q}\,(t))^{-1}\mathbf{x}\,(t) \end{aligned} \tag{1}$$

where $\dot{\mathbf{q}}\,(t) \in \mathbb{R}^n$ represents robot joint velocity vector, with n denoting the number of joints. $\mathbf{x}\,(t) \in \mathbb{R}^m$ is the velocity vector of the robot's m-dimensional robot end-effector in Cartesian space, and $\mathbf{J}(\mathbf{q}\,(t)) \in \mathbb{R}^{m\times n}$ corresponds to the Jacobian matrix.

A major limitation of the traditional inverse Jacobian method lies in its inability to handle situations when the robot operates near or at a singularity. From the perspective of linear equations, a robot approaching a singularity results in an ill-conditioned Jacobian matrix, where even a small $\mathbf{x}\,(t)$ can lead to disproportionately large $\dot{\mathbf{q}}\,(t)$, making the system sensitive to numerical errors. At a singularity, the equations may either have no solutions or infinitely many solutions.

To address the issues of singularities and redundancy, the pseudo-inverse of the Jacobian matrix can be calculated using the damped least squares method, as shown in the equation below:

$$\mathbf{J}(\mathbf{q})^{\dagger} = \mathbf{J}(\mathbf{q})^{T}\left(\mathbf{J}\,(\mathbf{q})\,\mathbf{J}(\mathbf{q})^{T} + \lambda_d{}^2\mathbf{I}\right)^{-1} \tag{2}$$

where $\lambda_d > 0$ is a small damping factor introduced to mitigate the effects of singularities. As the robot approaches a singularity, this damping term reduces the sensitivity of the system to ill-conditioned Jacobian.

Using the pseudo-inverse of the Jacobian matrix in Eq. (2), the inverse kinematics relation of the robot can be calculated:

$$\dot{\mathbf{q}}_{\mathrm{d}}\,(t) = \mathbf{J}(\mathbf{q})^{\dagger}\dot{\bar{\mathbf{x}}}\,(t) \tag{3}$$

where $\dot{\bar{\mathbf{x}}}\,(t)$ refers to the target velocity of the robot's end-effector corresponding to the virtual dynamics, and $\dot{\mathbf{q}}_{\mathrm{d}}\,(t)$ is the configuration space velocity to reach velocity $\dot{\bar{\mathbf{x}}}\,(t)$.

The pHRC module captures and abstracts the interactive relationship between the human operator and the robot. It defines the external force $\mathbf{f}_{\mathrm{ext}}$, as a combination of the feedback force generated by the operator $\mathbf{f}_{\mathrm{h}}$ and the force exerted by the environment on the robot $\mathbf{f}_{\mathrm{env}}$. This abstraction enables closed-loop control by interpreting the physical interaction as a force signal. During the collaboration process, the robot operates outside physical cages, sharing the workspace with the operator. However, environmental disturbances can manifest as random impacts on $\mathbf{f}_{\mathrm{ext}}$, potentially causing the robot to shake or make unintended movements. Consequently, the virtual dynamics model must not only adapt to the operator's intended traction forces but also actively resist such disturbances to ensure collaboration safety.

https://doi.org/10.1017/S0263574726103312 Published online by Cambridge University Press

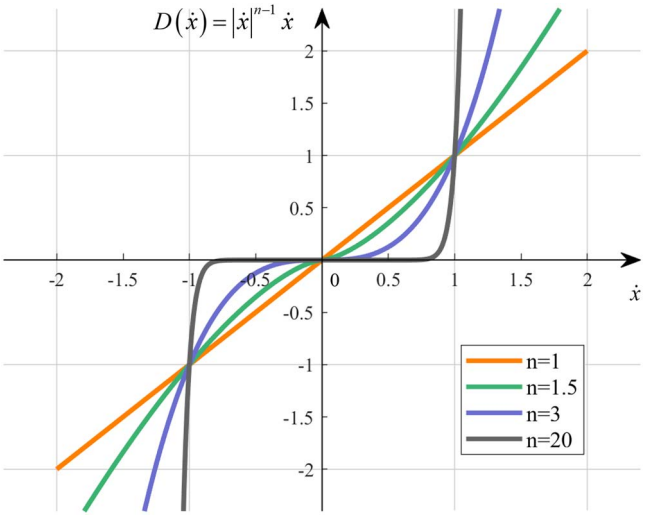


Figure 2. *The relationship between velocity (X-axis) and normalized nonlinear damping force(Y-axis).*

2.2. pHRC framework based on L-AC and SFC

As previously discussed, the L-AC algorithm can be employed to design the force control module. Given that the multi-dimensional motion of the robot can be represented as a linear superposition of single-dimensional motions [23], L-AC can be defined as follows:

$$m_A\ddot{x}(t) + \mu_A\dot{x}(t) = f_{\text{ext}}(t) \tag{4}$$

where m_A and μ_A denote the virtual inertia and damping parameters of the controller, respectively, both of which must be positive. The term $f_{\text{ext}}(t)$ represents the external force applied to the robot's end-effector, while $\ddot{x}$ and $\dot{x}$ denote the acceleration and velocity, respectively.

The relationship between the input and output of L-AC is linear, as indicated in Eq. (4). Consequently, L-AC cannot differentiate between traction and impact forces, which limits its effectiveness in resisting random impacts.

To overcome this limitation, a virtual dynamics control model based on shear-thickened fluid (STF) characteristics was proposed in ref. [23]. This model enables the robot to simulate the dynamics of solid–liquid phase transitions in STFs, behaving like a soft liquid under light contact while becoming rigid when subjected to strong impacts. The dynamic equation for this model can be expressed as follows:

$$m\ddot{x}(t) + \mu|\dot{x}(t)|^{n-1}\dot{x}(t) = f_{\text{ext}}(t) \tag{5}$$

where $D(\dot{x}) = \mu|\dot{x}|^{n-1}\dot{x}$ represents the nonlinear damping term, which can be derived from the constitutive equation of STFs. $m > 0$ is the virtual inertial term, and $\mu \geq 0$ a constant that characterizes the internal flow resistance properties of the material.

The principle behind the STF-based control is to indirectly adjust the nonlinear term within the controller through the external force f_{ext}, enabling the system to resist impacts while following the operator's traction. Specifically, the nonlinear damping term increases with the system's speed, allowing for rapid energy dissipation and enhanced impact resistance.

The behavior of the nonlinear damping force in relation to velocity is illustrated in Figure 2. The X-axis represents velocity $\dot{x}$, while the Y-axis shows the nonlinear damping force ($D(\dot{x}) = \mu|\dot{x}|^{n-1}\dot{x}$), with μ set to 1 and n taking values of 1, 1.5, 3, and 20. The function $D(\dot{x})$ is symmetric about the origin. For $n = 1$, the graph is a straight line, indicating that the control system reduces to linear admittance control. As $n > 1$, the curve steepens with increasing velocity, suggesting that when the system experiences a large external force impact, the damping force correspondingly increases to dissipate energy and maintain stability in human–robot interaction. It is important to note that while this effect becomes more pronounced with higher values of n, excessively high values may not always yield optimal performance.

https://doi.org/10.1017/S0263574726103312 Published online by Cambridge University Press

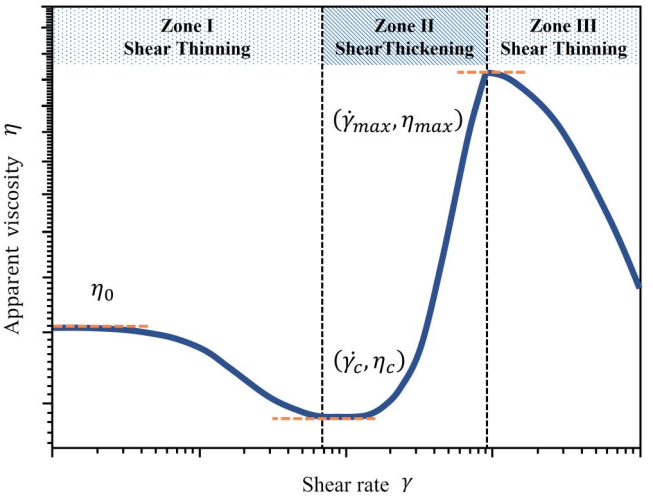


Figure 3. *Three phases of typical STFs and relevant parameters of its piecewise model. The X-axis represents shear rate $\dot{\gamma}$, while the Y-axis represents apparent viscosity η.*

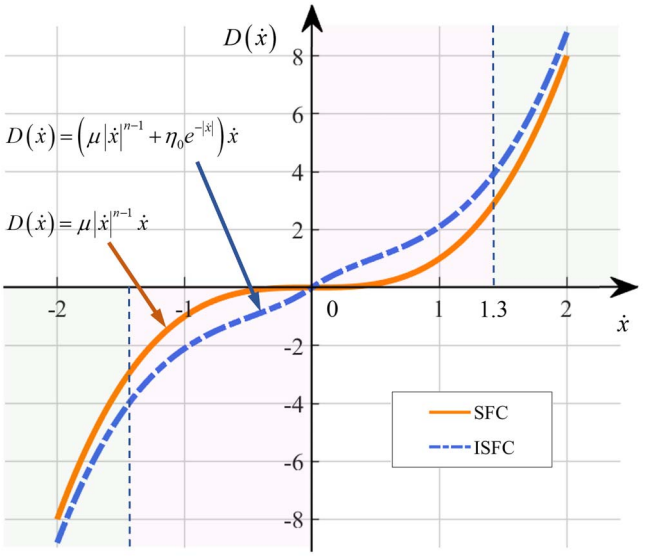


Figure 4. *Comparison of the effects of nonlinear damping forces in the ISFC and SFC with parameters $\mu = 1$, $n = 3$, and $\eta_0 = 5$.*

2.3. Limitations of designing virtual dynamics controller based on SFC

As previously mentioned, while LAC struggles to differentiate between traction and impact forces and effectively counter random impacts, the SFC successfully addresses these challenges. However, the SFC approach presents several limitations that require further investigation.

One issue with the SFC system is its delayed response when halting movement after the removal of traction force, which compromises the robot's ability to stop promptly in response to operator commands. Figure 2 illustrates nonlinear damping force behavior ($n > 1$) at low system velocities ($\dot{x} < 1$). The damping force significantly decreases as system speed diminishes, nearing negligible levels as velocity approaches zero. This effect is exacerbated with increasing values of n. Consequently, the system continues to move after traction force is removed, owing to the notably reduced energy dissipation capability of the SFC's near-zero damping term. This limitation adversely affects controller performance

https://doi.org/10.1017/S0263574726103312 Published online by Cambridge University Press

in pHRC, undermining the precise execution of operator-intended movements and potentially threatening the safety of both operators and robots. Further simulations and experiments will explore this phenomenon in detail.

Additionally, SFC is incompatible with dual-arm robot collaborative control algorithms, complicating its application in such systems. Precise task execution in dual-arm robots relies heavily on the relative positions and orientations of the end effectors. As noted, SFC-equipped robots cannot immediately halt after traction force is removed. This limitation hinders the ability to meet the stringent precision control requirements of dual-arm systems. For instance, when a human collaborates with dual-arm robots in material handling tasks, unintentional robotic movements can accumulate, significantly impairing system stability and potentially resulting in task failure.

This paper proposes an improvement to the existing SFC algorithm by incorporating the shear-thinning properties of shear-thickening fluids to address the aforementioned issues. This characteristic allows the system to maintain a certain level of nonlinear damping at low speeds, enabling the robot to quickly stop moving when traction is removed, thereby preserving system stability.

3. The design and safety validation of the ISFC

3.1. Design of the ISFC

As discussed earlier, the traditional SFC algorithm only considers the fluid characteristics during shear thickening, resulting in insufficient performance of the controller at low shear rates. According to ref. [25], the apparent viscosity of STFs exhibits three distinct zones as the shear rate increases: (1) shear thinning, (2) shear thickening, and (3) shear thinning again, as illustrated in Figure 3. In the initial phase ($\dot{\gamma} \le \dot{\gamma}_c$), as the shear rate increases, the STFs system exhibits shear-thinning behavior, causing the apparent viscosity to decrease from the initial value η_0 to the minimum value η_c. In the intermediate phase ($\dot{\gamma}_c \le \dot{\gamma} \le \dot{\gamma}_{\max}$), as the shear rate continues to increase, the fluid exhibits shear thickening behavior, causing the apparent viscosity to reach its peak value $\eta_{\max}$. Finally, in the third phase ($\dot{\gamma} \ge \dot{\gamma}_{\max}$), the apparent viscosity decreases dramatically. This paper argues that, in the low shear rate range, the SFC algorithm should account for the shear-thinning effect and the corresponding changes in apparent viscosity from a specific initial viscosity value.

The constitutive equation for Zone II of STFs can be modeled using the power-law model [24]:

$$\tau = \left(\mu|\dot{\gamma}|^{n-1} + a\right)\dot{\gamma} \tag{6}$$

where τ represents the stress tensor, $\eta = \mu|\dot{\gamma}|^{n-1} + a$ denotes the apparent viscosity, μ is a material-dependent constant, a is a curve adjustment parameter, $\dot{\gamma}$ is the shear rate, and n is the power-law index ($n > 1$).

Inspired by the constitutive Eq. (6), the shear thickening behavior is applied to the nonlinear damping term of the controller. $\dot{\gamma}$ and τ are replaced by $\dot{x}$ and $D(\dot{x})$, respectively. Based on the shear thinning characteristics of the fluid in Zone I of Figure 3, the adjustment parameter a is further defined as $a = \eta_0 e^{-|\dot{x}|}$. The dynamic equation of the controller's viscosity term, modeled using the improved shear-thickening fluid, is given by:

$$D(\dot{x}) = \left(\mu|\dot{x}|^{n-1} + \eta_0 e^{-|\dot{x}|}\right)\dot{x} \tag{7}$$

Combining Eq. (7) with Eq. (5), the proposed ISFC can be expressed as:

$$\begin{cases} m\ddot{x} + \left(\mu|\dot{x}|^{n-1} + \eta_0 e^{-|\dot{x}|}\right)\dot{x} = f_{\text{ext}} \\ \dot{\bar{x}} = \lambda\dot{x} \\ \bar{x} = \int \dot{\bar{x}}dt \end{cases} \tag{8}$$

where $D(\dot{x}) = \left(\mu|\dot{x}|^{n-1} + \eta_0 e^{-|\dot{x}|}\right)\dot{x}$ denotes the nonlinear damping term. $\eta_0 > 0$ is the initial value of the apparent viscosity when the fluid undergoes shear thinning behavior, λ is a gain term used to regulate the system output, and $\bar{x}$ is the output of the ISFC.

https://doi.org/10.1017/S0263574726103312 Published online by Cambridge University Press

The nonlinear damping term is derived from the constitutive equation of the fluid and incorporates two key components. First, $\mu|\dot{x}|^{n-1}$ represents a power-law model of apparent viscosity, characterizing the shear-thickening behavior of the fluid. This model enables the system to replicate the dynamic properties of STFs, ensuring both compliance and resilience against impacts. Second, $\eta_0 e^{-|\dot{x}|}$ accounts for viscosity variations, specifically modeling the shear-thinning behavior observed in Zone I of Figure 3. This modification addresses the limitation of inadequate damping force at low velocities, mitigating unpredictable movements in the system when the traction force from a human operator is withdrawn. Figure 4 presents a comparative analysis of the nonlinear damping terms between the proposed ISFC algorithm and the conventional SFC, with the parameter n set to 3. It can be observed that, within the velocity range close to zero (from -1.3 to 1.3), ISFC generates a higher damping force compared to SFC. This indicates that when the human collaborator withdraws the traction force, the proposed ISFC algorithm can dissipate the remaining energy of the system more rapidly, allowing the robot to comply with the human's intentions and reach the desired position.

The gain parameter λ is introduced to scale the velocity output according to the robot's operational constraints and human comfort levels, ensuring safe interaction velocities while maintaining system responsiveness.

3.2. Safety validation of the ISFC

The ISFC exhibits several essential properties – nonlinear velocity ratio, stability, and passivity – that ensure its practical applicability in robotic systems. The key characteristics are detailed as follows:

(1) Property 1: Nonlinear spatial velocity ratio.

Proof.

In the phase plane of a nonlinear system [26], the dynamics of the system in Eq. (8) can be represented as:

$$\begin{cases} \dot{p}_1 = p_2 \\ \dot{p}_2 = \frac{-\left(\mu|p_2|^{n-1}+\eta_0 e^{-|p_2|}\right)p_2}{m} \end{cases} \tag{9}$$

where p_1 represents the position state and p_2 the velocity state within the phase plane.

The spatial velocity ratio of the phase trajectory is given by:

$$R_{sv} = \frac{dp_2}{dt}\frac{dt}{dp_1} = \frac{\dot{p}_2}{\dot{p}_1} = -\frac{\mu|p_2|^{n-1} + \eta_0 e^{-|p_2|}}{m}. \tag{10}$$

From this equation, it is evident that when the velocity p_2 exceeds 1, the relative magnitude of the spatial velocity ratio of a linear ISFC system ($n = 1$) and a nonlinear ISFC system ($n > 1$) can be expressed as:

$$R_{sv}\,\big|_{p_2 \geq 1, n>1} \geq R_{sv}\,\big|_{p_2 \geq 1, n=1} \tag{11}$$

Thus, when the velocity is high ($p_2 \geq 1$), the spatial velocity of the nonlinear system ($n > 1$) is greater than that of the linear system ($n = 1$).

The spatial velocity ratio primarily investigates the convergence behavior of position and velocity states in the free motion stage. A larger nonlinear spatial velocity ratio indicates that the rate of change of velocity state ($dp_2/.dt$) is relatively faster than the rate of change of position state ($dp_1/.dt$) at a given point on the phase trajectory, which can ensure the stability of the system in the free state without external forces.

(2) Property 2: Stability.

Proof.

Consider the system described by Eq. (8), assuming that $m > 0$, $\mu > 0$, $n > 0$, and $\eta_0 > 0$ and a constant input force f_{ext}. Under these conditions, the system has a unique equilibrium point, which is globally asymptotically stable.

https://doi.org/10.1017/S0263574726103312 Published online by Cambridge University Press

Define:

$$f(\dot{p}) = \left(\mu|\dot{p}|^{n-1} + \eta_0 e^{-|\dot{p}|}\right)\dot{p} \tag{12}$$

Since $f(-\dot{p}) = -f(\dot{p})$, f is an odd-symmetric function. The derivative of $f(\dot{p})$ with respect to $\dot{p}$ is:

$$f'(\dot{p}) = \mu n|\dot{p}|^{n-1} + (1 - |\dot{p}|)\eta_0 e^{-|\dot{p}|} \tag{13}$$

In deriving Eq. (13), careful consideration is given to the piecewise nature of the absolute value function $|\dot{p}|$. For $\dot{p} \geq 0$, we have $|\dot{p}| = \dot{p}$ and $\frac{d}{d\dot{p}}|\dot{p}| = 1$. For $\dot{p} < 0$, we have $|\dot{p}| = -\dot{p}$ and $\frac{d}{d\dot{p}}|\dot{p}| = -1$. The derivation is first performed for the case $\dot{p} \geq 0$ and then extended to the entire domain using the odd symmetry property $f(-\dot{p}) = -f(\dot{p})$, which ensures the derivative $f'(\dot{p})$ is well-defined and positive under the given conditions for all $\dot{p} \in \mathbb{R}$.

We partition the domain into two intervals and analyze the strict positivity of $f'(\dot{p})$ in each. For $|\dot{p}| \leq 1$, both terms in $f'(\dot{p}) = \mu n|\dot{p}|^{n-1} + (1 - |\dot{p}|)\eta_0 e^{-|\dot{p}|}$ are non-negative: $\mu n|\dot{p}|^{n-1} \geq 0$ due to $\mu, n > 0$, and $(1 - |\dot{p}|)\eta_0 e^{-|\dot{p}|} \geq 0$ since $|\dot{p}| \leq 1$. At $\dot{p} = 0, f'(0) = \eta_0 > 0$; for $0 < |\dot{p}| \leq 1$, the sum remains strictly positive as both terms cannot vanish simultaneously. For $|\dot{p}| > 1$, define $t = |\dot{p}|$ and rewrite $f'(\dot{p}) \geq \mu n t^{n-1} - \eta_0 t e^{-t}$ (since $1 - t \geq -t$). The auxiliary function $g(t) = \mu n t^{n-1} - \eta_0 t e^{-t}$ satisfies $\lim_{t\to\infty} g(t) = +\infty$ due to exponential dominance ($\lim_{t\to\infty} \frac{\mu n t^{n-1}}{\eta_0 t e^{-t}} = +\infty$). Its derivative $g'(t) = \mu n(n-1)t^{n-2} + \eta_0(t-1)e^{-t}$ is positive for $t > 1$ because $\mu n(n-1)t^{n-2} > 0$ and $\eta_0(t-1)e^{-t} > 0$, rendering $g(t)$ strictly increasing. At the boundary $t = 1$, $g(1) = \mu n - \eta_0/e$, which is positive if $\mu n > \eta_0/e$. Consequently, $g(t) > 0$ for all $t > 1$, ensuring $f'(\dot{p}) > 0$ globally under this condition. By virtue of the strict monotonicity of $f(\dot{p})$ established above, there exists a unique solution $\dot{p}^*$ for any constant external force input f_{ext}.

By defining a new variable $s = \dot{p} - \dot{p}^*$, the equilibrium point is shifted to the origin, and the system becomes:

$$m\dot{s} + \left(\mu|s|^{n-1} + \eta_0 e^{-|s|}\right)s = 0 \tag{14}$$

Consider the Lyapunov function:

$$V(s) = s^2 \tag{15}$$

The derivative of V along the system trajectory is:

$$\dot{V}(s) = -\frac{2\left(\mu|s|^{n-1} + \eta_0 e^{-|s|}\right)s^2}{m} \tag{16}$$

Since $m > 0, \mu > 0, n > 0, \eta_0 > 0$, it can be seen that $\dot{V}(s)$ is negative definite. By Lyapunov's stability theorem, the system is globally asymptotically stable.

The ISFC must ensure that the robot's speed tracking is stable, enabling the robot to perform tasks such as human–robot collaboration involving dragging.

Stability ensures that the robot's movements remain consistent and controlled, even during tasks involving human–robot interaction and continuous external forces.

(3) Property 3: Passivity.

The stability of ISFC under constant external forces has been analyzed. To evaluate stability under other external force disturbances, energy dissipation must be considered. The passivity of the ISFC ensures the system does not accumulate energy uncontrollably, thereby enhancing reliability.

Proof.

Define a Lyapunov-like function:

$$\dot{U}(\dot{p}) = \frac{1}{2}m\,\dot{p}^2 \tag{17}$$

The system's power form is expressed as:

$$\frac{d}{dt}\left(\dot{U}(\dot{x})\right) = \dot{x}f_{ext} - h(\dot{x}) \tag{18}$$

https://doi.org/10.1017/S0263574726103312 Published online by Cambridge University Press

where $h(\dot{x}) = \left(\mu|\dot{x}|^{n-1} + \eta_0 e^{-|\dot{x}|}\right)\dot{x}^2$ represents the dissipated power. Since $h(\dot{x}) \geq 0$ and $1/2m\dot{x}^2$ has a lower bound, the system is dissipative. Furthermore, the non-negative dissipation term confirms that the system is passive.

During human–robot collaboration, disturbances or transitions from non-contact to contact states can occur. The passivity of ISFC ensures that external forces are dissipated, maintaining stability and safety.

3.3. Discretization of the ISFC

The ISFC discussed previously operates in continuous time; however, in practical applications, the constraints of hardware and software often necessitate the use of discrete time parameters. The discretized ISFC can be represented as follows:

$$\begin{cases} \ddot{x}(t) = m^{-1}\left(f_{ext}(t) - D\left(\dot{x}(t-\Delta t)\right)\right) \\ \dot{\bar{x}}(t) = \lambda\left(\dot{x}(t-\Delta t) + \ddot{x}(t)\,\Delta t\right) \\ \bar{x}(t) = x(t-\Delta t) + \dot{\bar{x}}(t)\,\Delta t \end{cases} \tag{19}$$

where Δt denotes the sampling time of the system, and the term $D\left(\dot{x}(t-\Delta t)\right)$ is defined as:

$$\left(\mu\,|\dot{x}(t-\Delta t)|^{n-1} + \eta_0 e^{-|\dot{x}(t-\Delta t)|}\right)\dot{x}(t-\Delta t)$$

By iterating Eq. (19) over discrete time steps, the discretized ISFC can compute the robot input $\bar{x}(t)$ at each step based on the current system state $\ddot{x}(t)$ and past information $\dot{x}(t-\Delta t)$. This approach facilitates the implementation of the controller in practical robot control systems with discrete-time updates.

4. Human-dual-arm robot collaboration framework based on ISFC

In this section, a human-dual-arm robot collaboration (HDRC) control framework is proposed, which integrates the ISFC algorithm into a dual-arm robot system. This framework facilitates the coordination between the dual-arm robot and the human operator to accomplish collaborative tasks. Unlike other studies that focus on force distribution in dual-arm and cooperative operations, the method presented here relies exclusively on natural force distribution, eliminating the need for specific force decomposition techniques.

To align the two robots with human intentions and maintain the pose relationship, we propose an HDRC control framework based on ISFC (Figure 5). This framework is designed to coordinate the asynchronous and unequal motions of the two robots, ensuring that their actions align with the operator's intent. Initially, the net force of the system is decomposed into the components $\mathbf{f}_{\text{ext1}}$ and $\mathbf{f}_{\text{ext2}}$ of the two robots, a process that does not necessitate precise modeling or control. Additionally, the component forces are converted into incremental poses $\bar{\mathbf{x}}_1$ and $\bar{\mathbf{x}}_2$ via the ISFC virtual dynamics model, where $\bar{\mathbf{x}} = \left[\begin{array}{cc} \bar{\mathbf{x}}' & \bar{\mathbf{x}}'' \end{array}\right] = \left[\begin{array}{cccccc} x & y & z & Rx & Ry & Rz \end{array}\right]$ represents the (6×1) pose vectors.

In this framework, we distinguish between two key concepts:

Virtual dynamic outputs: $(\bar{\mathbf{x}}_1, \bar{\mathbf{x}}_2)$ denote the raw pose adjustments generated by the ISFC controller based on external forces (Eq. 8). These outputs simulate the physical behavior of shear-thickening fluids, translating $\mathbf{f}_{\text{ext},i}$ into unprocessed Cartesian space displacements.

Incremental poses: $(\hat{\mathbf{x}}_1, \hat{\mathbf{x}}_2)$ represent the final coordinated commands sent to the robots. They are derived by combining virtual dynamic outputs $\bar{\mathbf{x}}_1, \bar{\mathbf{x}}_2$ with dual-arm synchronization logic and the reference trajectory (Eqs. 20 and 21), ensuring cooperative motion between manipulators.

The core of the framework is the HDRC control module, which facilitates the coordination of the two manipulators. When considering only positional synchronization, the module is defined as follows:

$$\begin{cases} \hat{\mathbf{x}}_1'(t) = \bar{\mathbf{x}}_1'(t) + {}^{E_1}_{B_1}\mathbf{R}\,{}^{B_1}_{W}\mathbf{R}\,{}^{W}_{B_2}\mathbf{R}\,{}^{B_2}_{E_2}\mathbf{R}\;\bar{\mathbf{x}}_2'(t-\Delta t) + \bar{\mathbf{x}}_{r1}' \\ \hat{\mathbf{x}}_2'(t) = \bar{\mathbf{x}}_2'(t) + {}^{E_2}_{B_2}\mathbf{R}\,{}^{B_2}_{W}\mathbf{R}\,{}^{W}_{B_1}\mathbf{R}\,{}^{B_1}_{E_1}\mathbf{R}\,\bar{\mathbf{x}}_1'(t-\Delta t) + \bar{\mathbf{x}}_{r2}' \end{cases} \tag{20}$$

https://doi.org/10.1017/S0263574726103312 Published online by Cambridge University Press

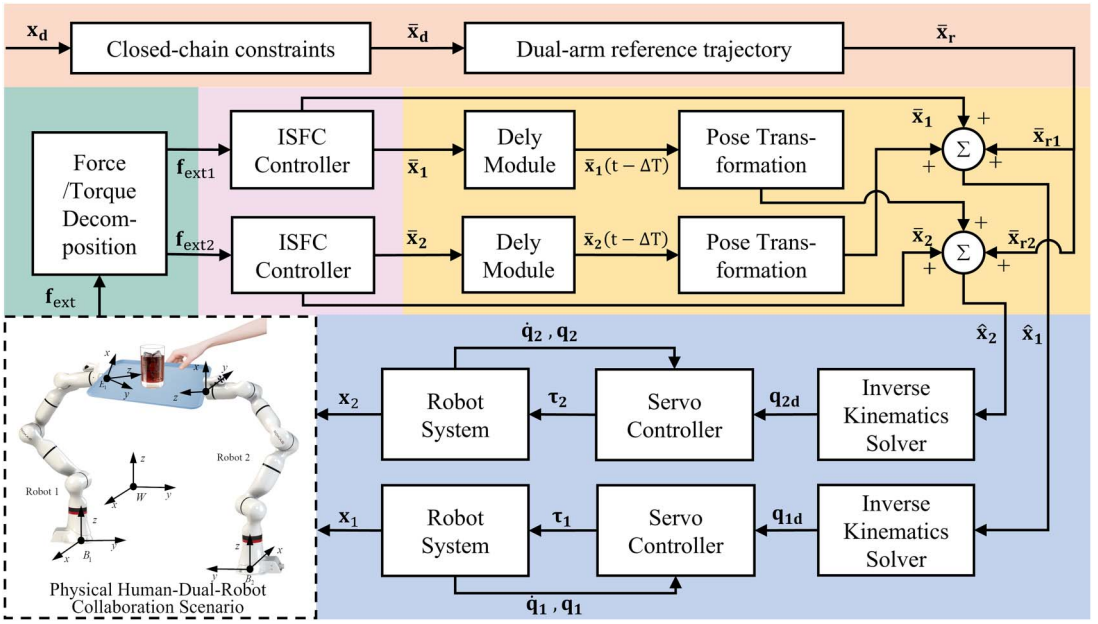


Figure 5. *A cooperative control framework for physical human-dual-arm robots based on ISFC, where $\bar{\boldsymbol{x}}_i$ (virtual dynamic output) is fed into the HDRC module to compute $\hat{\boldsymbol{x}}_i$ (incremental pose).*

where {W} denotes the world frame, $\{B_i\}$ and $\{E_i\}$ represent the base frame and end frame attached to robot i, respectively. $i = 1, 2$ indicates the i *th* manipulator. ${}^{A}_{B}\mathbf{R}$ represents rotation matrix of {B} relative to the {A}, and Δt signifies the sampling time. The vectors $\hat{\mathbf{x}}_i'$ and $\bar{\mathbf{x}}_i'$ denote the (3×1) position vectors.

The orientation calculations cannot be treated as a direct superposition, unlike the method described in Eq. (20). Instead, they must be computed through rotational matrix multiplication, as expressed in the following formulation:

$$\begin{cases} \boldsymbol{\Theta}\left(\hat{\mathbf{x}}_1''(\mathrm{t})\right) = {}^{B_1}_{E_1}\mathbf{R} \cdot \boldsymbol{\Theta}\left(\bar{\mathbf{x}}_1''(\mathrm{t}) + \bar{\mathbf{x}}_{r1}'' + {}^{E_1}_{E_2}\mathbf{R} \cdot \bar{\mathbf{x}}_2''(\mathrm{t}-\Delta\mathrm{t})\right) \\ \boldsymbol{\Theta}\left(\hat{\mathbf{x}}_2''(\mathrm{t})\right) = {}^{B_2}_{E_2}\mathbf{R} \cdot \boldsymbol{\Theta}\left(\bar{\mathbf{x}}_2''(\mathrm{t}) + \bar{\mathbf{x}}_{r2}'' + {}^{E_2}_{E_1}\mathbf{R} \cdot \bar{\mathbf{x}}_1''(\mathrm{t}-\Delta\mathrm{t})\right) \end{cases} \tag{21}$$

where $\hat{\mathbf{x}}_i''$ and $\bar{\mathbf{x}}_i''$ denote the (3×1) orientation vectors, while $\boldsymbol{\Theta}(\cdot)$ represents the transformation relationship from roll-pitch-yaw angle to the rotation matrix.

The external force applied to two robots generates virtual dynamic outputs $\bar{\mathbf{x}}_1$ and $\bar{\mathbf{x}}_2$ via the ISFC controller. In the HDRC framework, the input $\bar{\mathbf{x}}_1$ is combined with $\bar{\mathbf{x}}_2$ to produce the input $\hat{\mathbf{x}}_2$ for robot 2, utilizing both the delay module and the relative pose transformation module. The calculation process for robot 1 follows a similar approach. This methodology ensures a consistent compliance response of the dual-arm robot in response to external forces, maintaining the position and orientation relationship of the end-effectors.

The delayed superposition in Eqs. (20) and (21) implements a virtual mechanical coupling, where each arm responds to its partner's prior state $t - \Delta t$. This eliminates the explicit force distribution through pose feedback ${}^{B_2}_{E_2}\mathbf{R}$ transform, while reducing synchronization position errors (as shown in Figure 11f). The Δt term accounts for communication latency, preserving system causality.

The HDRC framework, as described by Eqs. (20) and (21), implements a virtual mechanical coupling between the dual arms through delayed pose superposition. To enhance the reproducibility of the proposed method, Algorithm 1 details the real-time implementation of the integrated ISFC and HDRC control scheme, illustrating the computational sequence executed at each sampling interval.

As shown in Algorithm 1, the control loop begins with the ISFC discrete update (Eq. (19)) that converts external forces into virtual dynamic outputs. Subsequently, the HDRC module computes the final

https://doi.org/10.1017/S0263574726103312 Published online by Cambridge University Press

Algorithm 1 Real-time ISFC + HDRC Control Loop

Require: $\mathbf{f}_{\text{ext},i}$ (measured force), $\mathbf{x}_i$ (current pose), Δt (sampling time)
Ensure: $\hat{\mathbf{x}}_i$ (incremental pose command for robot i)

for each sampling period k **do**
  for each robot $i = 1, 2$ **do**
    // ISFC discrete update (Equation. 19)
    $\dot{\mathbf{x}}_i[k] \leftarrow m^{-1}\left(\mathbf{f}_{\text{ext},i}[k] - D(\dot{\mathbf{x}}_i[k-1])\right)$
    $\dot{\bar{\mathbf{x}}}_i[k] \leftarrow \lambda \cdot \dot{\mathbf{x}}_i[k]$
    $\bar{\mathbf{x}}_i[k] \leftarrow \mathbf{x}_i[k-1] + \dot{\bar{\mathbf{x}}}_i[k] \cdot \Delta t$
    // HDRC coupling (Equations. 20−21)
    $\hat{\mathbf{x}}'_i[k] \leftarrow \bar{\mathbf{x}}'_i[k] + {}^{E}_{i}\mathbf{R}_{B_i} \cdot {}^{W}\mathbf{R}_{B_i} \cdot {}^{W}\mathbf{R}_{B_j} \cdot {}^{B_j}\mathbf{R}_{E_j} \cdot \bar{\mathbf{x}}'_j[k-1] + \bar{\mathbf{x}}'_{r,i}$
    $\hat{\mathbf{x}}''_i[k] \leftarrow \Theta\left(\bar{\mathbf{x}}''_i[k] \cdot {}^{E}_{i}\mathbf{R}_{B_i} \cdot {}^{W}\mathbf{R}_{B_i} \cdot {}^{W}\mathbf{R}_{B_j} \cdot {}^{B_j}\mathbf{R}_{E_j} \cdot \bar{\mathbf{x}}''_j[k-1]\right)$
  end for
  Send $\hat{\mathbf{x}}_1$, $\hat{\mathbf{x}}_2$ to robot controllers
end for

incremental poses by combining these outputs with delayed partner states through coordinate transformations. This approach ensures coordinated motion while maintaining the relative pose relationship between the dual arms.

It is crucial to highlight that the HDRC framework exclusively relies on natural force distribution, avoiding the need for specific force decomposition methods [27, 28], thereby enhancing the applicability of this approach across various scenarios.

5. Simulations and discussions

This section presents a comparative analysis of the dynamic characteristics of the proposed ISFC, the traditional SFC, and the L-AC in the time domain. According to Eq. (4), the L-AC applied to the controller can be specifically expressed as:

$$\begin{cases} m_{\text{A}}\ddot{x} + \mu_{\text{A}}\dot{x} = f_{\text{ext}} \\ \dot{\bar{x}} = \lambda_{\text{A}}\dot{x} \end{cases} \tag{22}$$

where λ_{A} denotes the gain parameter of L-AC. According to Eq. (5), the SFC applied to the controller can be expressed as:

$$\begin{cases} m_S\ddot{x} + \mu_S|\dot{x}|^{n_{\text{s}}-1}\dot{x} = f_{\text{ext}} \\ \dot{\bar{x}} = \lambda_{\text{S}}\dot{x} \end{cases} \tag{23}$$

where m_{S}, μ_{S}, λ_{S} denote, respectively, the virtual inertia, virtual damping, and gain parameter of SFC.

The ISFC applied to the controller can be formulated as follows:

$$\begin{cases} m\ddot{x} + \left(\mu|\dot{x}|^{n-1} + \eta_0 e^{-|\dot{x}|}\right)\dot{x} = f_{\text{ext}} \\ \dot{\bar{x}} = \lambda\dot{x} \end{cases} \tag{24}$$

where λ denotes the gain parameter of ISFC.

To objectively evaluate SFC's limitation in low-speed operation, we define three metrics for the system response after step removal of traction force at time t_0.

https://doi.org/10.1017/S0263574726103312 Published online by Cambridge University Press

Table I. *Parameters for ISFC, SFC, and L-AC.*

Controller type	**ISFC**	**SFC**	**L-AC**
Power law	$n = 3$	$n_S = 3$	$n_A = 1$
Scaled inertia	$m = 1$	$m_S = 1$	$m_A = 1$
Scaled damping	$\mu = 391$	$\mu_S = 391$	$\mu_A = 18$
Gain parameter	$\lambda = 0.19$	$\lambda_S = 0.19$	$\lambda_A = 1$
Improved damping	$\eta_0 = 5$	–	–
Sample time (s)	$\Delta t = 0.001$	$\Delta t = 0.001$	$\Delta t = 0.001$

1. **Convergence time** (T_{conv}): Time from t_0 until velocity satisfies $|\dot{x}(t)| \leq 0.001$m/s (duration to achieve near-stop).
2. **Residual displacement** (D_{res}): $\max |x(t) - x(t_0)|$ for $t \in [t_0, t_0 + T_{conv}]$ (unintended movement distance post-force removal).
3. **Overshoot ratio** (R_{over}): $\frac{\max |\dot{x}_{impact}(t)|/f_{impact}(t)}{\max |\dot{x}_{traction}(t)|/f_{traction}(t)}$, for $t \geq t_0$ (intensity of velocity fluctuation relative to max force).

The parameter settings for ISFC, SFC, and L-AC used in the simulations are detailed in Table I. The key parameters of the proposed ISFC, including the power-law index n, initial viscosity η_0, virtual inertia m, damping coefficient μ, gain λ, and sampling time Δt, are determined based on theoretical analysis of shear-thickening fluid dynamics and experimental validation, with reference to the parameter tuning framework for SFC in ref. [23].

1. **Power-law index** n: The power-law index n governs the shear-thickening effect of the nonlinear damping term. Following the logic in ref. [23], n is selected to balance impact resistance (high damping under large velocities) and low-speed compliance (moderate damping under small velocities). For typical traction forces ($f_{trac} \approx 5$ N) and impact forces ($f_{inter} \approx 50$ N) in human-dual-arm collaboration, $n = 3$ is determined using the ratio of force amplitudes and allowable velocities, ensuring the nonlinear damping term $\mu|\dot{x}|^{n-1}\dot{x}$ effectively suppresses high-speed impacts while maintaining smooth traction.
2. **Initial viscosity** η_0: The initial viscosity η_0 is introduced to address the low-speed stability defect of SFC (insufficient damping near zero velocity). Through iterative tests with η_0 in the range 1–10, $\eta_0 = 5$ is chosen because it minimizes residual displacement ($D_{res} \approx 4.6$ mm) and convergence time ($T_{conv} \approx 0.938$ s) when traction force is removed (Figure 7b), while avoiding excessive damping that hinders low-speed collaboration (Figure 4).
3. **Virtual inertia** m **and damping coefficient** μ: The virtual inertia $m = 1$ is normalized to simplify dynamics, consistent with the setup in [23]. The damping coefficient $\mu = 391$ is tuned to ensure the nonlinear damping term constrains impact-induced velocities within a safe range ($\dot{\tilde{x}} < 1$ m/s under $f_{ext} = 50$ N), validated via simulations in Figure 6a.
4. **Gain** λ **and sampling time** Δt: The gain $\lambda = 0.19$ scales the output velocity to match safe human–robot interaction limits (≤ 0.1 m/s). The sampling time $\Delta t = 0.001$ s (1000 Hz) is determined to match the robot's sampling period.

The input signals for the external force are given as $f_{ext} = \{1, 10, 50\}$. The relationships between the output velocities of each controller and time are illustrated in Figure 6. As observed, as the external force increases, the output velocities of both ISFC and SFC converge to a safe range ($\dot{\tilde{x}} < 1$ m/s), attributed to the nonlinear damping term's suppression of impacts. In contrast, the output velocity of the L-AC converges to nearly 3 m/s, which poses a risk for human operators. Furthermore, Figure 6c reveals a

https://doi.org/10.1017/S0263574726103312 Published online by Cambridge University Press

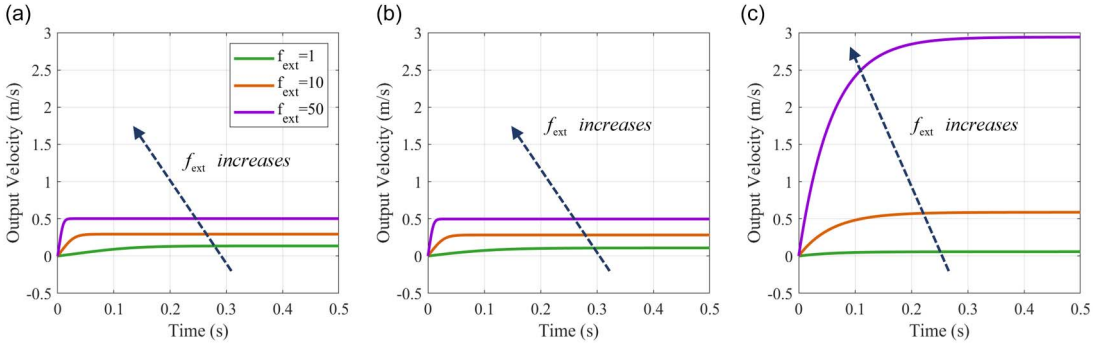


Figure 6. *The step responses of ISFC (a), SFC (b), and L-AC (c) in the time domain. The blue dashed arrow indicates the direction of increasing external force.*

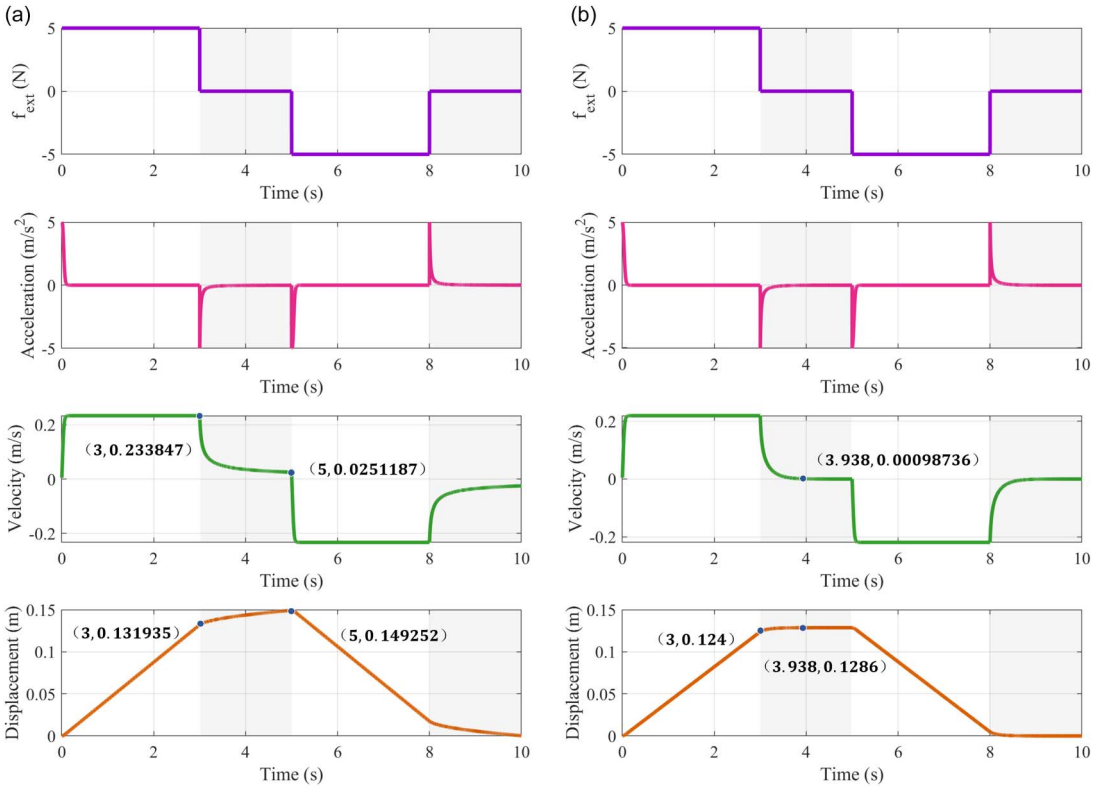


Figure 7. *The output acceleration, velocity, and displacement curves of SFC and ISFC under varying external force f_{ext}. (a) SFC. (b) ISFC.*

significant curve stratification phenomenon, indicating that the traditional L-AC struggles to manage sudden and substantial force impacts.

Additionally, the output acceleration, velocity, and displacement curves of the SFC and the proposed ISFC under varying external forces f_{ext} are presented in Figure 7. The external force input to the systems is expressed as:

$$f_{\text{ext}} = \begin{cases} 5 & , \ 0 \le t < 3\,s \\ 0 & , \ 3 \le t < 5\,s \\ -5 & , \ 5 \le t < 8\,s \\ 0 & , \ 8 \le t \le 10\,s \end{cases}$$

https://doi.org/10.1017/S0263574726103312 Published online by Cambridge University Press

Figure 7(a) and (b) compare the responses of SFC and ISFC under the varying force profile. Crucially, during traction force removal ($3 \leq t < 5$ s and $8 \leq t \leq 10$ s), SFC exhibits its low-speed stability defect: its output velocity decays slowly due to the near-zero nonlinear damping term at low speeds ($\dot{x} < 0.1$ m/s), resulting in significant residual displacement ($D_{\text{res}} \gg 17.3$ mm, simulated for $f_{\text{ext}} = 5$ n) and prolonged convergence time ($T_{\text{conv}} \gg 2$ s). In contrast, ISFC (Figure 7(b)) rapidly dissipates energy via its enhanced damping term $\eta_0 e^{-|\dot{x}|}\dot{x}$, driving the velocity to near zero swiftly ($T_{\text{conv}} \approx 0.938$ s) and minimizing unintended movement ($D_{\text{res}} \approx 4.6$ mm).

In summary, the simulation results demonstrate that the ISFC effectively manages impact forces while maintaining system stability at low velocities.

6. Experiments and discussions

6.1. Experimental setup

The experimental setup consists of two ROKAE xMate3 Pro 7-DOF manipulators, two KWR75B force/torque sensors (manufactured by Kunwei Sensing Technology), an industrial PC, and two Rochu grippers. The force sensors are mounted between the robot end flanges and the grippers, enabling direct measurement of the external forces $\mathbf{f}_{\text{ext},1}$ and $\mathbf{f}_{\text{ext},2}$ at each end-effector. This configuration allows the total external force acting on the system to be naturally distributed and measured without requiring explicit force decomposition algorithms. Operating at a sampling rate of 1,000 Hz, the sensors relay force information back to the controller. The controller comprises a control module, a dual-arm robot coordination module, and a communication module, with a total communication cycle of 0.001 s. Furthermore, output signals from the sensors undergo the load/gravity compensation algorithm, although this detail is not the primary focus of this paper.

6.2. Comparison of performance between ISFC, SFC, and L-AC for a single robot

In this experiment, the control parameters for ISFC, SFC, and L-AC remain consistent with those utilized in the simulations, as detailed in Table I. The maximum comfortable operating force f_h that is comfortable for a human operator to be approximately 3 N, while the impact force exerted by the robot is assumed not to exceed 30 N.

The experiment focuses on the simultaneous impact and traction phase, which comprehensively compares the performances of L-AC, SFC, and ISFC.

Simultaneous impact and traction phase: In this phase, to comprehensively assess the performance of the three control methods in handling both traction and impact forces, a traction force in the Y-axis positive direction allows easy robot pushing, with a sudden impact in the negative Z-axis during traction. Note that only forces are considered in these experiments, to prevent the cup from toppling due to potential changes in the robot's orientation. As shown in Figure 8, in the L-AC scenario, the coffee spills due to an external force impact, whereas in the SFC and ISFC scenarios, the coffee remains intact. Figure 9b illustrates that L-AC incurs a 0.23 m/s velocity jump, causing coffee spilling, while the peak velocities for SFC and ISFC are around 0.047 m/s, with gradual velocity remission post-impact, avoiding sudden jumps. This behavior stems from the dynamic characteristics of shear thickening in the nonlinear damping term. Figure 9 presents the velocity and position variations of the robot's end-effector. When subjected to a traction force not exceeding 2 N, the robot is pushed stably and smoothly, maintaining a velocity below 0.04 m/s, which demonstrates compliant response characteristics across all three control systems suitable for pHRC.

The limitation of SFC is quantitatively evident in Figure 9(e) and (h). Upon removal of the impact force at $t \approx 4.563$ s, SFC exhibits slow convergence ($T_{\text{conv}} = 8.29 \pm 0.55$ s, mean $\pm$ std, $n = 10$ trials, $f_{\text{impact}} \approx 18$ N), leading to substantial residual displacement ($D_{\text{res}} = 13.21 \pm 1.1$ mm) as the robot drifts unintentionally (Figure 8, Snapshot 4; Figure 9(e)). This drift poses a collision risk and impedes precise task execution. In stark contrast, ISFC (Figure 9(h,i)) achieves rapid stabilization ($T_{\text{conv}} = 0.50 \pm 0.08$ s)

https://doi.org/10.1017/S0263574726103312 Published online by Cambridge University Press

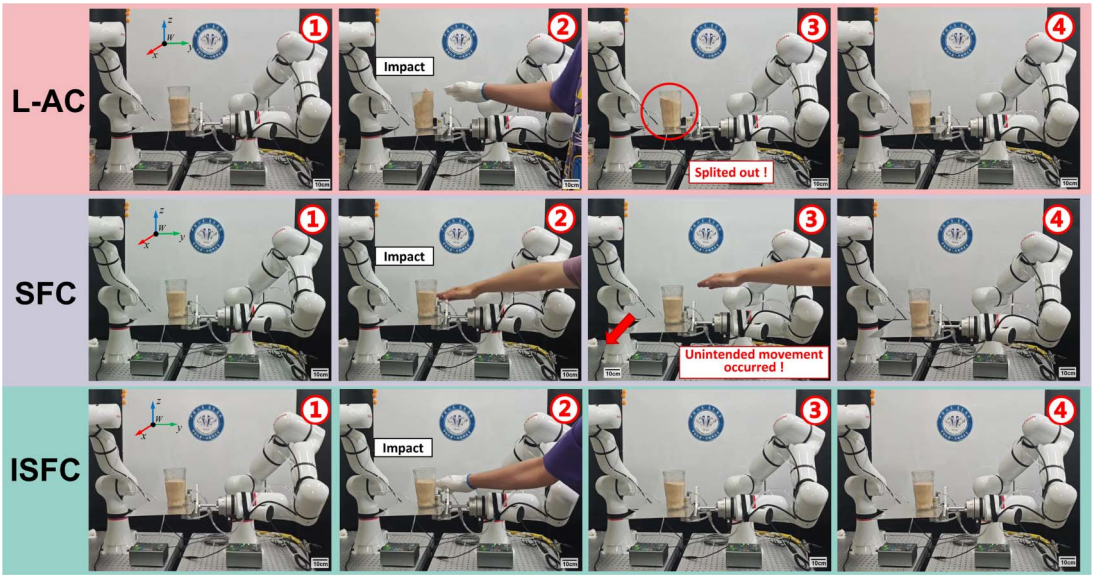


Figure 8. *Snapshots of the simultaneous impact and traction phase.*

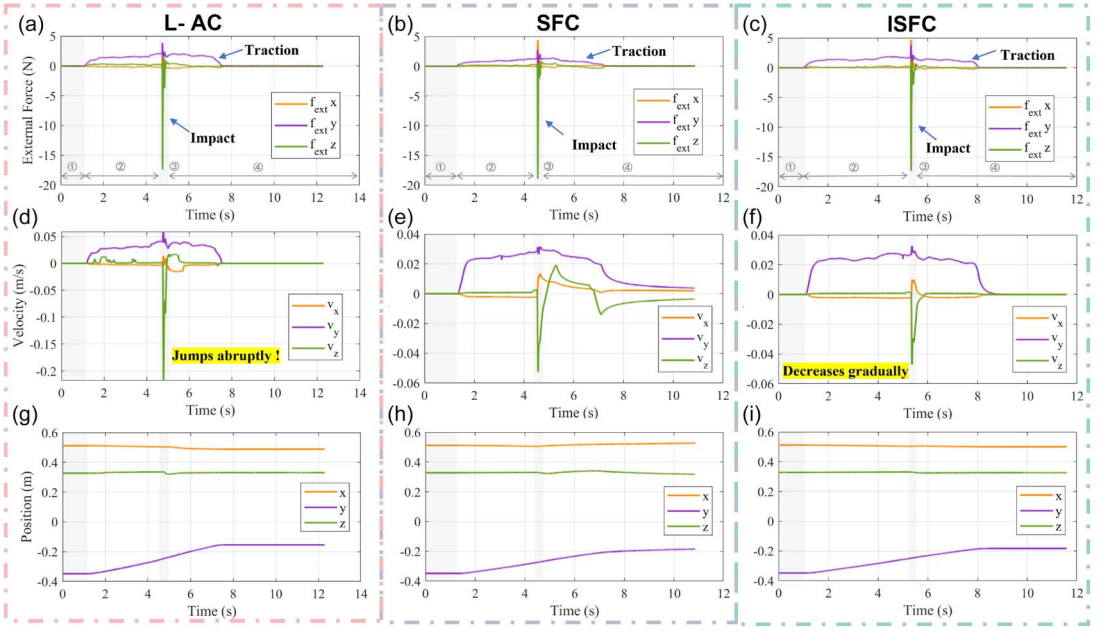


Figure 9. *The external force (Simultaneous impact and traction) acting on the manipulator during the impact phase, as well as the velocity and position of the end-effector. (a)–(c) L-AC. (d)–(f) SFC. (g)–(i) ISFC.*

with minimal residual displacement ($D_{\text{res}} = 6.7 \pm 0.3$ mm). While both controllers exhibit low overshoot ratios ($R_{\text{over}} = 0.28 \pm 0.02$ for SFC vs. 0.27 ± 0.01 for ISFC), the dramatic improvements in T_{conv} (94.1% reduction) and D_{res} (49.3% reduction) conclusively demonstrate ISFC's resolution of SFC's low-speed stability defect. These experimental metrics (Table II) align with the simulated behavior in Figure 7 and validate the efficacy of the $\eta_0 e^{-|\dot{x}|}$ damping term.

https://doi.org/10.1017/S0263574726103312 Published online by Cambridge University Press

Table II. *Experimental comparison of low-speed stability metrics (SFC vs. ISFC, $f_{ext} \approx 18N$, $n = 10$ trials).*

Metric	SFC	ISFC	Improvement
Convergence time	8.29 ± 0.55 s	0.50 ± 0.08 s	$\downarrow 94.1\%$
Residual displacement	13.21 ± 1.1 mm	6.7 ± 0.3 mm	$\downarrow 49.3\%$
Overshoot ratio	0.42 ± 0.05	0.31 ± 0.04	$\downarrow 26.2\%$

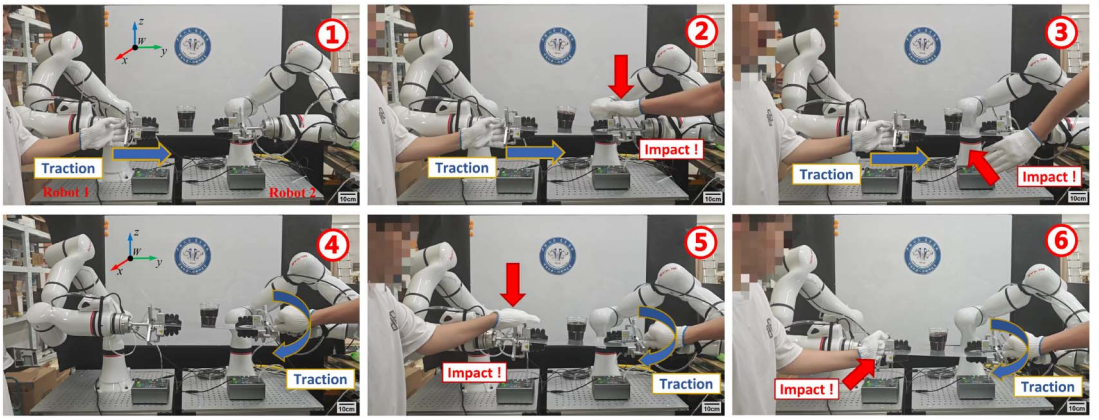


Figure 10. *Snapshots of the traction phase of HDRC.*

In conclusion, the proposed ISFC algorithm can be effectively applied in pHRC, resisting random impacts and maintaining low-velocity stability. These advantages are attributed to the nonlinear damping term of the ISFC, which accounts for viscosity changes during shear thinning in shear-thickening fluids (STFs). This allows the system to maintain relatively high damping at low velocities, preventing unintended movements of the robot, as quantitatively demonstrated by the 94% reduction in convergence time and 49% reduction in residual displacement compared to SFC (Table II).

6.3. Comparison of performance between ISFC, SFC, and L-AC for a dual-arm robot

Traction and Impact Phase of HDRC: As illustrated in Figure 10, snapshots are presented from the experimental phase of the cooperative water-carrying traction phase between robots and a human operator. Impacts are randomly applied to the end-effectors of Robot 1 and Robot 2.

The experimental results are depicted in Figure 11. The external forces are denoted as $\mathbf{f}_{\text{ext1}}$ and $\mathbf{f}_{\text{ext2}}$, as illustrated in Figure 11(a) and (b). The trajectories of the two robots' end-effectors are depicted in Figure 11(c), consistent with the snapshots shown in Figure 10. The controller proposed in Section IV enables dual-arm robot to collaborate with human to complete tasks. Furthermore, the output velocities of the two robots, as illustrated in Figure 11(d) and (e), demonstrate a positive correlation with the external forces, indicating that the robots can respond smoothly to the intentions of the human operator.

The fluctuations in velocity observed in Figure 11(d) and (e) result from these impacts. Notably, despite the presence of impacts, the peak velocity generated remains within the safe range for human–robot collaboration, not exceeding 0.1 m/s. To further illustrate the advantages of the algorithm, the concept of position synchronous error is introduced. In this paper, position synchronous error is defined as the difference between the positions of Robot 1 and Robot 2 at each communication cycle, with the initial position deviation subtracted. The position synchronous errors of the two robots in the X, Y, and Z directions are illustrated in Figure 11f. The position synchronous error is less than 8 mm, indicating excellent synchronization performance of the controller. The error reaches its maximum when

https://doi.org/10.1017/S0263574726103312 Published online by Cambridge University Press

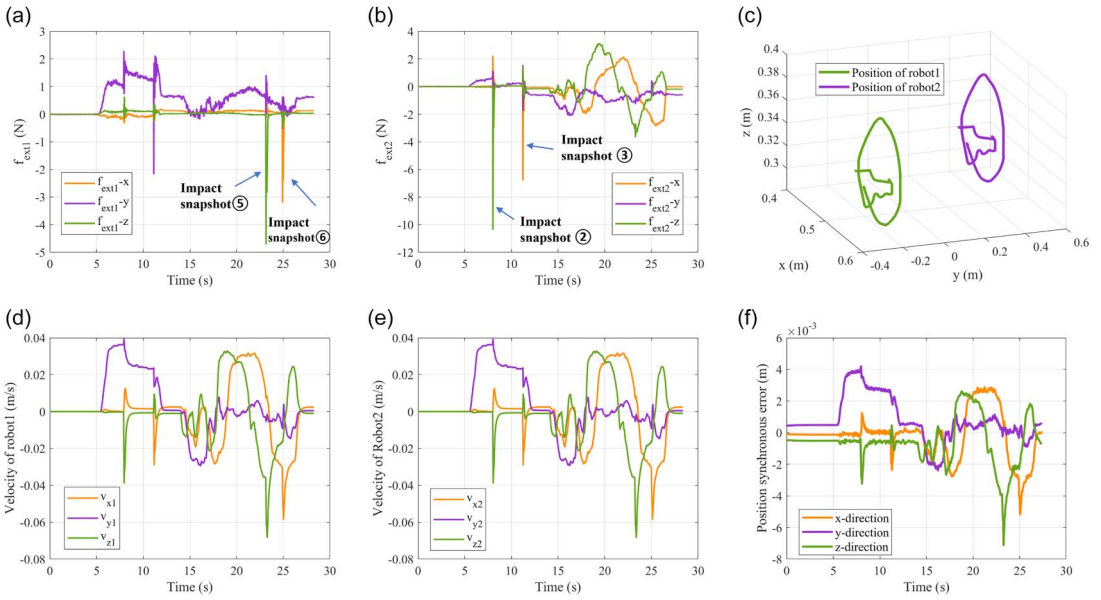


Figure 11. *The results of the collaborative traction and impact phase between the dual-arm robot and the human operator. (a) and (b) External forces f_{ext1} and f_{ext2}. (c) Three-dimensional positions of robots 1 and 2. (d) and (e) Output velocities of robots 1 and 2. (f) Position synchronous error.*

the absolute value of the instantaneous velocity is highest, with a peak of 7.05 mm in the *Z*-direction. However, once the impact dissipates, the position synchronous error decreases to a lower numerical range. Moreover, the position synchronous error is positively correlated with the output velocity, which is due to the limitations of the system's communication cycle.

The experimental results demonstrate that the proposed ISFC algorithm effectively resists random impacts and maintains stability under low-velocity conditions. When integrated with the HDRC framework, the ISFC can be deployed on dual-arm robots to achieve stable operations that are resilient to impacts, thereby facilitating reliable collaboration between human operators and dual-arm robots in the presence of disturbances.

7. Conclusion

In this paper, we propose an Improved SFC that accounts for changes in the apparent viscosity of shear-thickening fluids during shear thinning, representing this effect as an additional damping term in the algorithm. This controller enables the robot to move and stop in accordance with the human operator's intentions while withstanding random impacts. Additionally, we introduce a human-arm robot collaboration framework based on the ISFC.

To contextualize the contributions of ISFC within the broader landscape of advanced control strategies, we provide a comparative analysis against three prominent approaches:

1. **Compared to adaptive impedance/admittance control** [17–19]: ISFC achieves comparable adaptability to human intentions without requiring real-time parameter estimation. Its nonlinear damping term inherently suppresses impact disturbances (e.g., reducing velocity overshoot by 94% vs. L-AC in Figure 9), whereas adaptive methods often rely on explicit collision detection modules [20] that introduce latency. During impacts, ISFC constrains end-effector velocity to <0.1 m/s (Figure 9g–i), aligning with ISO/TS 15,066 safety limits.
2. **Compared to optimization-based controllers** [1, 4]: ISFC attains similar impact resistance (peak velocity ≤ 0.047 m/s under 30N impacts, Figure 9) and dual-arm coordination precision

https://doi.org/10.1017/S0263574726103312 Published online by Cambridge University Press

(synchronization error <8 mm, Figure 11f) while avoiding computational optimization overhead. This enhances real-time feasibility in dynamic human–robot collaboration scenarios.

3. **Compared to hybrid force-position control** [27, 28]: Unlike methods requiring precise force decomposition models, ISFC leverages natural force distribution through physics-inspired dynamics (Section IV). This simplifies implementation while ensuring stability during disturbances, evidenced by rapid post-impact convergence (0.5 s vs. SFC's 8.29 s, Table II) and minimal residual displacement (6.7 mm vs. SFC's 13.21 mm).

The core distinction of ISFC lies in the following: By encoding shear-thickening/thinning properties directly into control laws, it intrinsically reconciles impact resistance and low-speed stability – a capability typically requiring multi-layer architectures in model-based approaches. This biomimetic design enables passive-aggressive compliance (yielding to traction while resisting impacts) with minimal computational cost.

Despite these advancements, certain limitations remain that warrant further investigation, which will guide future research directions. First, the controller parameters determined in this study were based on simulations and can be further optimized in subsequent work. Furthermore, the HDRC framework currently addresses only the positional coordination of the two manipulators; future research could explore human–robot collaboration for tasks involving orientation changes.

Supplementary material. The supplementary material for this article can be found at https://doi.org/10.1017/S0263574726103312.

Author contributions. Siwen Zhang, Jinjun Duan, and Yiming Bin conceived and designed the study. Siwen Zhang and Chendong Wu were responsible for data collection and statistical analysis. Siwen Zhang wrote the article. Siwen Zhang, Chendong Wu, and Tingyan Du assisted with the structure and language of the manuscript. All authors read and approved the final manuscript.

Financial support. This work was supported by the National Youth Science Foundation of China under Grant No. 52205017, the Aviation Foundation under Grant No. 2022Z050052001, and the Jiangsu Funding Program for Excellent Postdoctoral Talent under Grant No. 2023ZB052.

Competing interests. The authors declare no conflicts of interest exist.

Ethical approval. Not applicable.

References

[1] K.-C. Ying, P. Pourhejazy, C.-Y. Cheng and Z.-Y. Cai, "Deep learning-based optimization for motion planning of dual-arm assembly robots," *Comput. Ind. Eng.* **160**, 107603 (2021).
[2] S. Zhang, Y. Chen, J. Zhang and Y. Jia, "Real-Time Adaptive Assembly Scheduling in Human-multi-robot Collaboration According to Human Capability," **In:** *2020 IEEE International Conference on Robotics and Automation (ICRA)* (IEEE, 2020) pp. 3860–3866.
[3] Z. Chen, Q. Guo, T. Li, Y. Yan and D. Jiang, "Gait prediction and variable admittance control for lower limb exoskeleton with measurement delay and extended-state-observer," *IEEE Trans. Neural Netw. Learn. Syst.* **34**(11), 8693–8706 (2022).
[4] Y. Ren, Z. Zhou, Z. Xu, Y. Yang, G. Zhai, M. Leibold, F. Ni, Z. Zhang, M. Buss and Y. Zheng, "Enabling versatility and dexterity of the dual-arm manipulators: A general framework toward universal cooperative manipulation," *IEEE Trans. Robot.* **40**, 2024–2045 (2024).
[5] J. Zhu, M. Gienger, G. Franzese and J. Kober, "Do you need a hand? – a bimanual robotic dressing assistance scheme," *IEEE Trans. Robot.* **40**, 1906–1919 (2024).
[6] C. Meng, T. Zhang, D. Zhao and T. L. Lam, "Fast and comfortable robot-to-human handover for mobile cooperation robot system," *Cyborg Bionic Syst.* **5**, 0120 (2024).
[7] X. Wang, S. Guo, Z. Xu, Z. Zhang, Z. Sun and Y. Xu, "A robotic teleoperation system enhanced by augmented reality for natural human–robot interaction," *Cyborg Bionic Syst.* **5**, 0098 (2024).
[8] R. Wen, Q. Rouxel, M. Mistry, Z. Li and C. Tiseo, "Collaborative bimanual manipulation using optimal motion adaptation and interaction control: Retargeting human commands to feasible robot control references," *IEEE Robot. Autom. Mag.* **31**(4), 68–80 (2023).
[9] A. Bauer, D. Wollherr and M. Buss, "Human–robot collaboration: A survey," *Int. J. Hum. Robot.* **5**(01), 47–66 (2008).

https://doi.org/10.1017/S0263574726103312 Published online by Cambridge University Press

[10] A. Calanca, R. Muradore and P. Fiorini, "A review of algorithms for compliant control of stiff and fixed-compliance robots," *IEEE/ASME Trans. Mechatron.* **21**(2), 613–624 (2015).
[11] A. Q. L. Keemink, H. Van der Kooij and A. H. A. Stienen, "Admittance control for physical human–robot interaction," *Int. J. Robot. Res.* **37**(11), 1421–1444 (2018).
[12] N. Hogan, "Impedance control of industrial robots," *Robot. Cim-INT. Manuf.* **1**(1), 97–113 (1984).
[13] C. Ott, *Cartesian Impedance Control of Redundant and Flexible-Joint Robots* (Springer, 2008).
[14] R. J. Adams and B. Hannaford, "Stable haptic interaction with virtual environments," *IEEE Trans. Robot. Autom.* **15**(3), 465–474 (1999).
[15] K. Hashtrudi-Zaad and S. E. Salcudean, "Analysis of control architectures for teleoperation systems with impedance/admittance master and slave manipulators," *Int. J. Robot. Res.* **20**(6), 419–445 (2001).
[16] N. Hogan, "Impedance control: An approach to manipulation: Part II—Implementation," *J. Dyn. Syst. Meas. Control* **107**(1), 8–16 (1985).
[17] W. He, C. Xue, X. Yu, Z. Li and C. Yang, "Admittance-based controller design for physical human–robot interaction in the constrained task space," *IEEE Trans. Autom. Sci. Eng.* **17**(4), 1937–1949 (2020).
[18] Y. Shen, B. Li, W. Tian, J. Duan and M. Liu, "Human–robot collaborative assembly of movable airfoils using adaptive admittance control," *J. Intell. Manuf. Spec. Equip.* **3**(2), 204–216 (2022).
[19] C. Wu, Y. Shen, G. Li, P. Li and W. Tian, "Compliance Auxiliary Assembly of Large Aircraft Components Based on Variable Admittance Control," **In:** *Intelligent Robotics and Applications: 14th International Conference, ICIRA 2021, Yantai, China, October 22–25, 2021, Proceedings, Part II 14* (Springer, Yantai, China, 2021) pp. 469–479.
[20] S. Haddadin, A. De Luca and A. Albu-Schäffer, "Robot collisions: A survey on detection, isolation, and identification," *IEEE Trans. Robot.* **33**(6), 1292–1312 (2017).
[21] G. Lin, J. Yu and J. Liu, "Adaptive fuzzy finite-time command filtered impedance control for robotic manipulators," *IEEE Access* **9**, 50917–50925 (2021).
[22] B. V. Adorno, P. Fraisse and S. Druon, "Dual Position Control Strategies Using the Cooperative Dual Task-space Framework," **In:** *2010 IEEE/RSJ International Conference on Intelligent Robots and Systems* (IEEE, 2010) pp. 3955–3960.
[23] L. Chen, L. Chen, X. Chen, H. Lu, Y. Zheng, J. Wu, Y. Wang, Z. Zhang and R. Xiong, "Compliance while resisting: A shear-thickening fluid controller for physical human–robot interaction," *Int. J. Robot. Res.* **43**(11), 1731–1769 (2024).
[24] M. Wei, K. Lin and L. Sun, "Shear thickening fluids and their applications," *Mater. Design* **216**, 110570 (2022).
[25] M. Li, B. Lyu, J. Yuan, C. Dong and W. Dai, "Shear-thickening polishing method," *Int. J. Mach. Tools Manuf.* **94**, 88–99 (2015).
[26] J.-J. E. Slotine and W. Li, Applied Nonlinear Control, Prentice Hall, Englewood Cliffs, NJ, USA, 1991, 459 pp.
[27] F. Caccavale, P. Chiacchio, A. Marino and L. Villani, "Six-DOF impedance control of dual-arm cooperative manipulators," *IEEE/ASME Trans. Mechatron.* **13**(5), 576–586 (2008).
[28] S. Erhart and S. Hirche, "Internal force analysis and load distribution for cooperative multi-robot manipulation," *IEEE Trans. Robot.* **31**(5), 1238–1243 (2015).

Cite this article: S. Zhang, J. Duan, K. Gui, Y. Bin, C. Wu, Y. Yu, T. Du, Z. Wang, L. Wang and H. Wu (2026). "Enabling physical human/dual-arm collaboration to resist random impacts: An improved shear-thickening fluid controller", Robotica **44**, 764–782. https://doi.org/10.1017/S0263574726103312

https://doi.org/10.1017/S0263574726103312 Published online by Cambridge University Press